NETWORKS AND HETEROGENEOUS MEDIA
©American Institute of Mathematical Sciences
Volume **5**, Number **3**, September **2010**

doi:10.3934/nhm.2010.5.583

pp. **583–602**

# MODELING MULTIPHASE NON-NEWTONIAN POLYMER FLOW IN IPARS PARALLEL FRAMEWORK

Changli Yuan, Mojdeh Delshad and Mary F. Wheeler

Center for Subsurface Modeling
The University of Texas at Austin
Austin, TX 78712, USA

Abstract. With the depletion of oil reserves and increase in oil price, enhanced oil recovery methods such as polymer flooding to increase oil production from waterflooded fields are becoming more attractive. Effective design of these processes is challenging because the polymer chemistry has a strong effect on reaction and fluid rheology, which in turn has a strong effect on fluid transport. Polymer flow characteristics modeled in the UT-Austin IPARS (Integrated Parallel Accurate Reservoir Simulator) are adsorption on rock surfaces, polymer viscosity as a function of shear rate, polymer and electrolytes concentrations, permeability reduction, and inaccessible pore volume. A time-splitting algorithm is used to "independently" solve advection, diffusion/dispersion, and chemical reactions.

1. **Introduction.** Numerical simulation of multiphase flow and reactive transport in porous media includes a rich collection of coupled nonlinear processes with multiple spatial and temporal scales. These models are widely applied in petroleum engineering, groundwater hydrology, environmental engineering and chemical engineering. Significant mathematical and computational challenges are imposed by realistic simulations for simultaneous convection, diffusion, dispersion, and chemical reactions. An interesting example that is attracting much interest in the petroleum industry is polymer flooding. This enhanced oil recovery process has been used for many years to increase the efficiency of water flooding through greater volumetric sweep efficiency and reducing channeling and early water breakthrough. It is well known that polymer flooding increases oil recovery by increasing the water viscosity and reducing permeability. Many researchers also suggest that polymer flooding may reduce the relative permeability of the water phase [2, 8, 23]. Recent studies show that the polymer flooding residual oil saturation is lower than the waterflood residual oil saturation, when polymer flooding is employed right after primary production or at early stages of waterflooding [10]. Polymer is characterized by specific bulk properties such as rheology, solubility, and molecular weight. The rheology of a polymer is indicative of its physical characteristics. A well-established polymer rheological model [6] has been implemented into the Multiphase Reactive Transport Module (TRCHEM) in the Integrated Parallel Accurate Reservoir Simulator (IPARS) [18]. Non-Newtonian polymer viscosity including polymer and electrolyte

2000 *Mathematics Subject Classification.* Primary: 76A05, 76S05, 65Y05; Secondary: 80A50.
*Key words and phrases.* Polymer flooding, Non-Newtonian fluid, Coupling flow and chemistry, Parallel computation.
The first author is supported by NSF grant 0835745.

concentrations effects, polymer adsorption on rock surfaces, effective permeability and pore volume are taken into account.

2. **Two-phase flow in porous media.** The governing equations for two-phase flow in porous media are given by

$$\frac{\partial(\phi N_o)}{\partial t} - \nabla \cdot [\rho_o \overrightarrow{\overrightarrow{K}} \frac{k_{ro}}{\mu_o}(\nabla P_o - \rho_o g \nabla D)] = q_o, \tag{1}$$

$$\frac{\partial[\phi \rho_w (1 - N_o/\rho_o)]}{\partial t} - \nabla \cdot \{\rho_w \overrightarrow{\overrightarrow{K}} \frac{k_{rw}}{\mu_w}[\nabla(P_o - P_c) - \rho_w g \nabla D]\} = q_w, \tag{2}$$

where $N$ is concentration, $\rho$ is density, $P$ is pressure, $q$ is a source/sink term, $k_r$ is relative permeability, $\mu$ is viscosity, $P_c$ is capillary pressure, $\phi$ is porosity, $\overrightarrow{\overrightarrow{K}}$ is a permeability tensor, $g$ is magnitude of gravity, and $D$ is depth. The subscripts $o$ and $w$ denote the oil phase and the water phase, respectively. The governing equations are solved over a spatial domain $\Omega$ for $t > 0$. Initial and boundary conditions are specified to close the system. The governing equations are discretized in space by the expanded mixed finite element method [1] using the lowest order Raviart Thomas spaces defined over a rectangular grid. The backward Euler method is used in time discretization. The discretization details are outlined in [16] and [20]. The nonlinear system of equations arising at each time step is solved fully implicitly by a Newton iteration with a multistage preconditioned GMRES linear solver [11].

3. **The reactive transport.**

3.1. **Mass conservation law.** The mass conservation law is described for a species in a stationary phase and flowing phases. More precisely, the mass balance of species $i$ in stationary phase $s$ is given by

$$\frac{\partial[(1-\phi)c_{is}]}{\partial t} = R^I_{is} + R^C_{is} + R^N_{is}, \tag{3}$$

where $c_{is}$ is concentration of species $i$ in stationary phase. The source terms include contributions from interphase transfer $R^I$, chemical reaction $R^C$ and radionuclide decay $R^N$, all functions of the concentrations. Details regarding the source terms can be found in [15].

The mass balance of species $i$ in flowing phase $\alpha$ is written as

$$\frac{\partial(\phi c_{i\alpha} S_\alpha)}{\partial t} + \nabla \cdot (c_{i\alpha} \overrightarrow{u}_\alpha - \phi S_\alpha \overrightarrow{\overrightarrow{D}}_{i\alpha} \nabla c_{i\alpha}) = R^I_{i\alpha} + \phi S_\alpha R^C_{i\alpha} + \phi S_\alpha R^N_{i\alpha} + q_{i\alpha}, \tag{4}$$

where $\alpha = o, w$ denotes the flowing phase. $S_\alpha$ and $\overrightarrow{u}_\alpha$ are saturation and Darcy velocity of phase $\alpha$, respectively. $c_{i\alpha}$ is concentration of species $i$ in phase $\alpha$. $q_{i\alpha}$ is injection/production rate for species $i$ in phase $\alpha$. The diffusion-dispersion tensor $\overrightarrow{\overrightarrow{D}}_{i\alpha}$ is the sum of molecular diffusion and mechanical dispersion. The molecular diffusion $\overrightarrow{\overrightarrow{D}}^{mol}_{i\alpha}$ and mechanical dispersion $\overrightarrow{\overrightarrow{D}}^{disp}_{i\alpha}$ are given by

$$\overrightarrow{\overrightarrow{D}}^{mol}_{i\alpha} = \frac{d^{mol}_{i\alpha} \overrightarrow{\overrightarrow{I}}}{\tau}, \tag{5}$$

$$\phi S_\alpha \overrightarrow{\overrightarrow{D}}^{disp}_{i\alpha} = d_{t,\alpha} |\overrightarrow{u}_\alpha| \overrightarrow{\overrightarrow{I}} + (d_{l,\alpha} - d_{t,\alpha}) \frac{\overrightarrow{u}_\alpha \overrightarrow{u}^T_\alpha}{|\overrightarrow{u}_\alpha|}, \tag{6}$$

where $d_{i\alpha}^{mol}$, $d_{t,\alpha}$, and $d_{l,\alpha}$ are molecular diffusivity, transverse and longitudinal dispersivities for species $i$ in phase $\alpha$. $\tau$ is the tortuosity of porous media. $\overrightarrow{u}_{\alpha}^{T}$ is the transpose of the flux vector $\overrightarrow{u}_{\alpha}$. $\overrightarrow{\overrightarrow{I}}$ is an identity matrix.

3.2. **Phase-summed transport equations.** Assuming a linear partitioning of species between flowing phases

$$c_{i\alpha} = \Gamma_{i\alpha} c_{ir}, \tag{7}$$

where $\Gamma_{i\alpha}$ is a constant partitioning coefficient and $r$ refers to the reference phase. Since the species simulated in the polymer flooding (polymer, anion, and divalent cations) only exist in the water phase and we assume water is always present, we choose the water phase as the reference phase.

Summing equation (4) over the flowing phases and noting that the net interphase transfer is zero, i.e., $\sum_{\alpha} R_{i\alpha}^{I} + R_{i}^{A} = 0$ , we obtain the phase-summed transport equation for species $i$ in the flowing phases

$$\frac{\partial(\phi_i^* c_{iw})}{\partial t} + \nabla \cdot (c_{iw} \overrightarrow{u}_i^* - \overrightarrow{\overrightarrow{D}}_i^* \nabla c_{iw}) = R_i^{TC} + R_i^{TN} - R_i^{A} + q_i^{T}, \tag{8}$$

where $R_{\alpha}^{A}$ is the net mass transfer into (positive) or out of (negative) rock. The following phase summed variables are defined for convenience

$$\phi_i^* = \phi \sum_{\alpha} \Gamma_{i\alpha} S_{\alpha}, \quad \overrightarrow{u}_i^* = \sum_{\alpha} \Gamma_{i\alpha} \overrightarrow{u}_{\alpha}, \quad \overrightarrow{\overrightarrow{D}}_i^* = \phi \sum_{\alpha} S_{\alpha} \Gamma_{i\alpha} \overrightarrow{\overrightarrow{D}}_{i\alpha}$$

$$R_i^{TC} = \phi \sum_{\alpha} S_{\alpha} R_{i\alpha}^{C}, \quad R_i^{TN} = \phi \sum_{\alpha} S_{\alpha} R_{i\alpha}^{N}, \quad q_i^{T} = \sum_{\alpha} q_{i\alpha}.$$

Equation (8) is solved by applying a time splitting algorithm, which is presented in the following section.

3.3. **Time splitting algorithm.**

3.3.1. *Time stepping.* In general the time step in a flow model is different from the concentration time step. The flow time step is usually larger than the concentration time step. Given that the solutions of the flow model (pressure, saturations and velocities etc.) are available at $t^n$ and $t^{n+1}$ and the concentrations of all species are available at $t^m$, the concentrations at time $t^{m+1}$ need to be computed. Assuming that $(t^m, t^{m+1}) \subset (t^n, t^{n+1})$, equation (8) is discretized in time as

$$\begin{aligned} &\frac{T_i^{m+1} - T_i^{m}}{\triangle t} + \nabla \cdot (c_{iw}^{m} \overrightarrow{u}_i^{*,m+1/2} - \overrightarrow{\overrightarrow{D}}_i^{*,m} \nabla c_{iw}^{m+1}) \\ =&R_i^{TC,m+1/2} + R_i^{TN,m+1/2} - R_i^{A,m+1/2} + q_i^{T,m+1/2}, \end{aligned} \tag{9}$$

where $\triangle t = t^{m+1} - t^{m}$, $T_i = \phi_i^* c_{iw}$; and $\phi_i^*$ and $\overrightarrow{u}_i^*$ at $t \in (t^m, t^{m+1})$ are computed by linear interpolation between the known values at $t^n$ and $t^{n+1}$. Direct solution of equation (9) is practically impossible. Therefore a time-splitting algorithm is used to "independently" solve the advection, diffusion/dispersion, and chemical reaction, which means each subproblem delivers intermediate values of $T_i$ as $\bar{T}_i$, $\hat{T}_i$ and $T_i^{m+1}$. The individual steps of this algorithm are briefly described below. More details about this algorithm can be found in [4, 19, 20].

3.3.2. *Advection.* The equation solved in the advection step is of the form

$$\frac{\partial(\phi_i^* c_{iw})}{\partial t} + \nabla \cdot (c_{iw} \overrightarrow{u}_i^*) = q_i^T. \tag{10}$$

Equation (10) is solved by a high order Godunov method with slope limiting. Let $T_i^m = \phi_i^{*,m} c_{iw}^m$, then $\bar{T}_i$ is explicitly computed from

$$\frac{\bar{T}_i - T_i^m}{\triangle t} + \nabla \cdot (\overrightarrow{u}_i^{*,m+1/2} c_{iw}^m) = q_i^{T,m+1/2}. \tag{11}$$

The intermediate values of concentrations after the advection step are computed as

$$\bar{c}_{iw} = \bar{T}_i / \phi_i^{*,m+1}. \tag{12}$$

3.3.3. *Chemical reaction.* For kinetic chemical reaction, we solve

$$\frac{\partial(\phi_i^* c_{iw})}{\partial t} = R_i^{TC}, \tag{13}$$

by standard explicit ODE integration. Currently, three schemes are implemented: the forward Euler first-order scheme, second-order Runge-Kutta and fourth-order Runge-Kutta. If the forward Euler first-order scheme is used, equation (13) becomes

$$\frac{\hat{T}_i - \bar{T}_i}{\triangle t} = R_i^{TC,m+1/2}. \tag{14}$$

The radionuclide decay reaction and the adsorption can be treated as chemical reactions. In this case, equation (14) becomes

$$\frac{\hat{T}_i - \bar{T}_i}{\triangle t} = R_i^{TC,m+1/2} + R_i^{TN,m+1/2} - R_i^{A,m+1/2}. \tag{15}$$

3.3.4. *Diffusion/Dispersion.* In the diffusion/dispersion step, the following equation is discretized in space by an expanded mixed finite method and implicitly solved using a GMRES preconditioner [19].

$$\frac{\partial(\phi_i^* c_{iw})}{\partial t} + \nabla \cdot (\overrightarrow{\overrightarrow{D}}_i^* \nabla c_{iw}) = 0. \tag{16}$$

The equation after discretizing in time is given by

$$\frac{T_i^{m+1} - \hat{T}_i}{\triangle t} - \nabla \cdot (\overrightarrow{\overrightarrow{D}}_i^{*,m} \nabla c_{iw}^{m+1}) = 0. \tag{17}$$

4. **Modeling polymer properties.** The numerical modeling of polymer flooding is based on the following assumptions:

- The process is isothermal;
- No polymer degradation such as chemical, mechanical, and biological degradation is modeled;
- There are no chemical reactions related to polymer;
- The polymer only exists in the water phase;
- The polymer does not change the density of water phase;
- The polymer does not affect the rock porosity, which means the volume of the adsorbed polymer is negligible;
- The polymer is treated as a mono-species without molecular weight distribution, so no chromatographic phenomenon occurs in the porous media;
- The adsorption of polymer on the rock surface is assumed to be in local equilibrium.

4.1. **Adsorption.** Polymer adsorption is assumed irreversible with the polymer concentration and reversible with the salt concentration. A Langmuir-type isotherm model is used to describe the polymer adsorption onto the rock surface [9]. The adsorbed concentration is a function of the polymer concentration, salinity, and permeability given by

$$\hat{C}_p = min\left(\tilde{C}_p, \frac{a_4(\tilde{C}_p - \hat{C}_p)}{1 + b_4(\tilde{C}_p - \hat{C}_p)}\right), \tag{18}$$

where $\tilde{C}_p$ is the overall polymer concentration which is the sum of polymer in the water phase and the adsorbed polymer, and $\hat{C}_p$ is the adsorbed polymer concentration. The units of polymer concentration and adsorbed polymer concentration are in $wt\%$ (weight percentage) polymer in the water phase. The minimum in equation (18) is taken to guarantee the mass balance. The ratio $a_4/b_4$ determines the maximum adsorption level and $b_4$ controls the curvature of the isotherm adsorption curve. The parameter $a_4$ is calculated from

$$a_4 = (a_{41} + a_{42}C_{SEP})\sqrt{\frac{k_{ref}}{k}}, \tag{19}$$

where $b_4$, $a_{41}$, and $a_{42}$ are input parameters obtained from matching laboratory polymer adsorption data. Here $k_{ref}$ is the reference permeability at which the input adsorption parameters are specified and $C_{SEP}$ is the effective salinity defined as

$$C_{SEP} = max(C_{anion} + (\beta - 1)C_{d-cation}, C_{SE1}), \tag{20}$$

where $C_{anion}$ and $C_{d-cation}$ are the total anion concentration and the total divalent cations concentration in the aqueous phase in units of $meq/ml$. The influence of divalent ions such as $Ca^{2+}$ and $Mg^{2+}$ on polymer properties is more pronounced than that of monovalent ions ($Na^{+}$ and $K^{+}$), because of their higher charge and polarizability [17]. The input parameter $\beta$ is measured in the laboratory and reflects the influence of divalent cations on the polymer properties compared to that of monovalent cations. $C_{SE1}$ is an input tolerance parameter for the effective salinity.

4.2. **Viscosity.** The modified Flory-Huggins equation [7] is used to calculate the polymer viscosity at very low shear rates

$$\mu_p^0 = \mu_w[1 + (A_{p1}C_p + A_{p2}C_p^2 + A_{p3}C_p^3)C_{SEP}^{S_p}], \tag{21}$$

where $\mu_p^0$ is the polymer viscosity at low shear rate, $\mu_w$ is the aqueous phase viscosity, $A_{p1}$, $A_{p2}$, and $A_{p3}$ are input parameters obtained from experiments. The factor $C_{SEP}^{S_p}$ represents the dependence of polymer viscosity on salinity and hardness. The effective salinity, $C_{SEP}$, is given by equation (20). $S_p$ is an input parameter corresponding to the slope of $\frac{\mu_p^0 - \mu_w}{\mu_w}$ versus $C_{SEP}$ on a log-log plot.

Meter's equation [14] is used to model the shear thinning behavior of a polymer solution. The apparent viscosity of a polymer solution, $\mu_p$, is given by

$$\mu_p = \mu_w + \frac{\mu_p^0 - \mu_w}{1 + (\frac{\dot{\gamma}}{\dot{\gamma}_{1/2}})^{P_\alpha - 1}}, \tag{22}$$

where $\dot{\gamma}_{1/2}$ and $P_\alpha$ are input parameters. The in-situ shear rate is modeled by the modified Blake Kozeny capillary bundle equation [13, 17]

$$\dot{\gamma} = \frac{\dot{\gamma}_c |\overrightarrow{u}_w|}{\sqrt{\bar{k} k_{rw} \phi S_w}}, \tag{23}$$

where $\dot{\gamma}_c$ is an empirical shear rate coefficient obtained from laboratory experiments, that accounts for non-ideal effects such as slip at the pore walls [17, 22]. The average permeability $\bar{k}$ (in unit of $Darcy$) is calculated from

$$\bar{k} = \left[ \frac{1}{k_x} \left( \frac{u_w^x}{|\overrightarrow{u}_w|} \right)^2 + \frac{1}{k_y} \left( \frac{u_w^y}{|\overrightarrow{u}_w|} \right)^2 + \frac{1}{k_z} \left( \frac{u_w^z}{|\overrightarrow{u}_w|} \right)^2 \right], \tag{24}$$

where $|\overrightarrow{u}_w|$ (in unit of $ft/day$) is the magnitude of the Darcy velocity for the water phase in each element and is computed as

$$|\overrightarrow{u}_w| = \sqrt{(u_w^x)^2 + (u_w^y)^2 + (u_w^z)^2}. \tag{25}$$

An alternative calculation of $|\overrightarrow{u}_w|$ is available for wellblocks and is given by

$$|\overrightarrow{u}_w| = \frac{|q_w|}{2\pi r_{w,eff} L}, \tag{26}$$

where $q_w$ is the volumetric flow rate for each wellblock, $L$ is the length of the open wellbore, and $r_{w,eff}$ is the effective well radius input parameter with the default value of well radius. This alternative wellblock flux reduces the grid effect on the shear rate and subsequent viscosity calculations.

4.3. **Permeability reduction.** The total mobility reduction of a polymer solution is measured by the resistance factor, $R_F$, defined as the ratio of the injectivity of water to that of a single-phase polymer solution flowing under the same conditions [12]; that is

$$R_F = \frac{k_w/\mu_w}{k_p/\mu_p} = \frac{k_w}{k_p} \cdot \frac{\mu_p}{\mu_w}, \tag{27}$$

where $k_w$ is the effective permeability of water, $k_p$ is the effective permeability of polymer solution. To measure the permeability reduction effect alone, a permeability reduction factor $R_k$ is defined as

$$R_k = \frac{k_w}{k_p}. \tag{28}$$

The permeability reduction caused by polymer solution is irreversible and is an indicator of the degree of channel blocking of polymer solution. This permanent effect is called the residual resistance factor, $R_{RF}$, defined as

$$R_{RF} = \frac{mobility\ before\ polymer\ flood}{mobility\ after\ polymer\ flood}. \tag{29}$$

Here $R_{RF}$ is nearly equal to $R_k$, but $R_F$ is generally much larger than $R_k$. The permeability reduction factor $R_k$ is modeled as

$$R_k = 1 + \frac{(R_{kmax} - 1) b_{rk} C_p}{1 + b_{rk} C_p}, \tag{30}$$

where

$$R_{kmax} = min \left( \left[ 1 - \frac{c_{rk} (A_{p1} C_{SEP}^{S_p})^{1/3}}{(\sqrt{k_x k_y}/\phi)^{1/2}} \right]^{-4}, rkcut \right), \tag{31}$$

with $c_{rk}$ and $b_{rk}$ input parameters obtained from laboratory measurements. The input parameter $rkcut$ is used as the upper limit of permeability reduction. The viscosity of the aqueous phase is multiplied by $R_k$ to account for permeability reduction.

4.4. **Inaccessible pore volume.** Dawson and Lantz first reported that polymer molecules travel faster than other species in water phase, when the polymer retention is low [5]. Many laboratory experiments have confirmed this phenomenon [21] [3]. Dawson and Lantz named this phenomenon an inaccessible pore volume (IPV). An input constant, the effective pore volume $\phi_e$, used to model the inaccessible pore volume effect, is defined as

$$\phi_e = 1 - IPV. \tag{32}$$

The porosity in the conservation law for polymer species is multiplied by the effective pore volume. Then the conservation law (4) for polymer becomes

$$\frac{\partial(\phi\phi_e c_{i\alpha} S_\alpha)}{\partial t} + \nabla\cdot(c_{i\alpha}\overrightarrow{u}_\alpha - \phi\phi_e S_\alpha \overrightarrow{\overrightarrow{D}}_{i\alpha}\nabla c_{i\alpha}) = R^I_{i\alpha} + \phi\phi_e S_\alpha R^C_{i\alpha} + \phi\phi_e S_\alpha R^N_{i\alpha} + q_{i\alpha}. \tag{33}$$

Equation (33) is discretized following a similar procedure described in Section 3 using operator time-splitting.

5. **Numerical results.** The results of polymer modeling were first verified with the UTCHEM simulator [6]. We then compared results of polymer flood simulations for different grid resolutions.

5.1. **Verification.** A 3D heterogeneous anisotropic reservoir with an unconfined inverted 5-spot well pattern is modeled for verification and results are compared with those obtained from the IMPEC chemical flood simulator, UTCHEM. All boundaries are closed to flow. Figure 1 shows the permeability distribution and well locations. Table 1 gives the reservoir description and fluid properties. The effects of molecular and mechanical dispersion and capillary pressure are neglected. The imbibition Brooks-Corey type relative permeability curve for water/oil flow is given by

$$k_{r\alpha} = k^0_{r\alpha}(S_{n\alpha})^{n_\alpha}, \quad \alpha = w, o, \tag{34}$$

where $k^0_{r\alpha}$ is the relative permeability endpoint for phase $\alpha$. Here $n_\alpha$ is the relative permeability exponent and $S_{n\alpha}$ is the normalized phase saturation defined by

$$S_{n\alpha} = \frac{S_\alpha - S_{\alpha r}}{1 - S_{wr} - S_{or}}, \quad \alpha = w, o, \tag{35}$$

and $S_{wr}$ and $S_{or}$ are residual water and residual oil saturations, respectively.

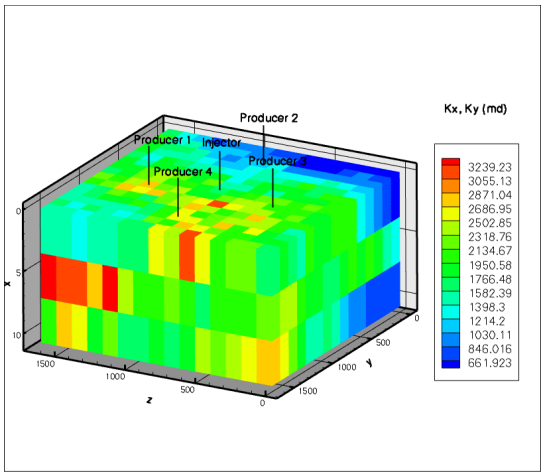


FIGURE 1. Permeability distribution and well locations for the verification case

TABLE 1. Reservoir description and fluid properties for the verification case

| Parameters | Values |
|---|---|
| $\Omega$ $[ft]$ | 1640.5x1640.5x10.8 |
| grids | 15x15x3 |
| $S_{wirr}$, $S_{or}$ | 0.2, 0.2 |
| $k^0_{rw}$, $k^0_{ro}$ | 0.2, 1.0 |
| $n_w$, $n_o$ | 1.5, 2.0 |
| $P_{o,init}$ $[psi]$ | 967.06 |
| $S_{o,init}$ | 0.62 |
| $\rho_w, \rho_o$ $[lb/ft^3]$ | 62.5, 55.6 |
| $\mu_w, \mu_o$ $[cp]$ | 0.73, 40.0 |
| $c_{anion,init}$ and $c_{d_cation,init}$ $[meq/ml]$ | 0.00831, 0.00551 |
| $d^{mol}_{i\alpha}$ $[ft^2/day]$ | 0 |
| $d_{t,\alpha}$ and $d_{l,\alpha}$ $[ft]$ | 0, 0 |

The polymer solution is continuously injected with a variable flow rate for 742 days followed by a chase water flood. The injection rate and polymer concentration grading are shown in Figures 2 and 3. The producers are pressure constrained with bottomhole pressure of 300 $psi$. The wells penetrate through the entire reservoir thickness. Table 2 gives the polymer model input parameters.

The injection bottomhole pressure, the cumulative oil recovery, and the effluent polymer concentration are shown in Figures 4 through 6. Similar results were obtained using IPARS and UTCHEM.

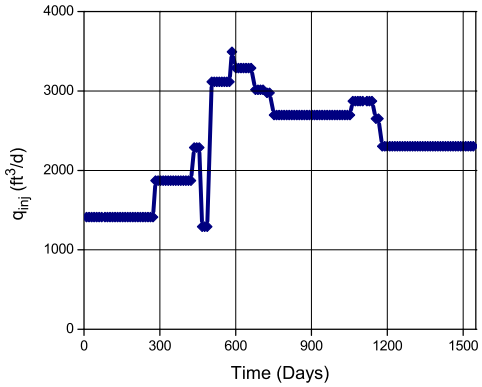


FIGURE 2. Injection rate for the verification case

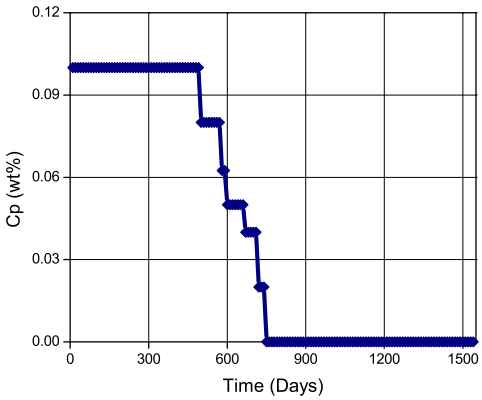


FIGURE 3. Polymer concentration grading for the verification case

TABLE 2. Polymer model input parameters for the verification case

| **Parameters** | **Values** |
|---|---|
| $a_{41}$, $a_{42}$, $b_4$ | 8.66, 0.0, 100 |
| $b_{rk}$, $c_{rk}$ | 100, 0.2 |
| $\beta$ | 20 |
| $S_p$ | -0.3 |
| $C_{SE1}$ $[meq/ml]$ | 0.01 |
| $\dot{\gamma}_{1/2}$ $[sec^{-1}]$, $\dot{\gamma}_c$, $P_\alpha$ | 280, 130, 2.2 |
| $\phi_e$ | 0.85 |
| $A_{p1}$, $A_{p2}$, $A_{p3}$ | 38.47, 1600, 0 |
| $c_{anion,inj}$ and $c_{d_cation,inj}$ $[meq/ml]$ | 0.00831, 0.00551 |

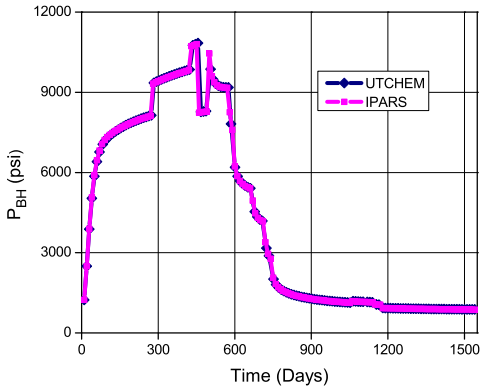


FIGURE 4. Injection bottomhole pressure for the verification case

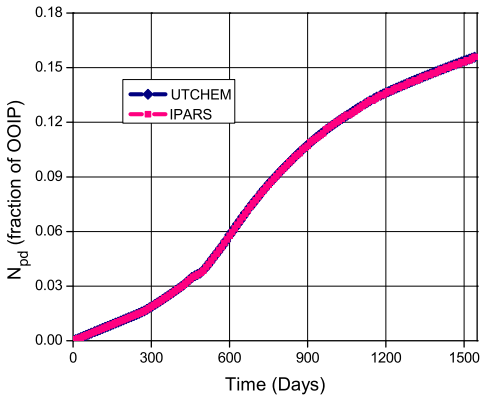


FIGURE 5. Cumulative oil recovery for the verification case

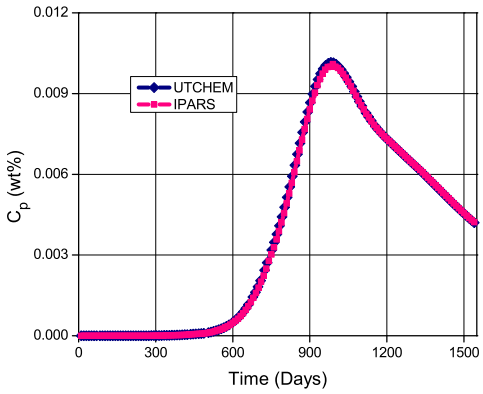


FIGURE 6. Effluent polymer concentration in producer No. 1 for the verification case

5.2. **Scale-up simulations.** In this section, we compare the simulation results of seven different grids generated for an anisotropic heterogeneous reservoir described in Table 3. The reservoir dimensions are slightly different, while the total pore volumes and original oil in place are kept the same. The simulation grid block sizes vary from 150 x 150 x 2 $ft$ (coarsest grid) to 18.75 x 18.75 x 2 $ft$ (finest grid). The initial oil saturation is 0.8 and the reservoir is at hydrostatic equilibrium. The permeability, porosity distributions, residual water and oil saturations are upscaled from the finest grid data based on a single-phase scale-up scheme. Capillary pressure is neglected and a Brooks-Corey type relative permeability is used.

TABLE 3. Grid description and computation time

| | **Grids** | **Total Elements** | **Active Elements** | **Processors** | **CPU time** (hr) |
|---|---|---|---|---|---|
| Grid01 | 86x94x19 | 153596 | 112480 | 16 | 9.53 |
| Grid02 | 43x47x19 | 38399 | 28120 | 4 | 1.56 |
| Grid03 | 22x24x19 | 10032 | 7220 | 1 | 0.37 |
| Grid04 | 11x12x19 | 2508 | 1900 | 1 | 0.05 |
| Grid05 | 43x47x10 | 20210 | 14800 | 2 | 1.45 |
| Grid06 | 43x47x5 | 10105 | 7400 | 1 | 1.21 |
| Grid07 | 22x24x10 | 5280 | 3800 | 1 | 0.16 |

There are 10 injectors and 7 producers forming multiple 7-spot well patterns. The wells are partially penetrated. The well locations are adjusted so that every well is located in the center of each element. Figure 7 shows the permeability distributions and the well locations for Grid01 and Grid04. The permeability distribution for the different grids is different due to the single-phase scaleup procedure. The injectors are rate constrained. The producers are pressure constrained with the bottomhole pressure of 300 $psi$. The injection starts with a water preflush for 300 days (about 4 $PV$) until the overall water cut from all producers reaches 0.98; a slug with 0.15 $wt\%$ polymer is then injected for 220 days (about 1 $PV$) at a lower injection rate; followed by a water postflush for 80 days.

These simulations were performed on Bevo, a parallel cluster located at the Institute for Computational Engineering and Sciences at the University of Texas at Austin. Bevo has 90 dual-core AMD Athlon processors with a core frequency of 2.00 GHz and memory of 2 GB per core. The number of processors and the CPU time used are also shown in Table 3. The parallel computation scalability is tested on grid02 and the result is shown in Table 4 indicating nearly linear speedup.

TABLE 4. Parallel computation scalability

| **Processors** | **CPU time** (hr) |
|---|---|
| 4 | 1.56 |
| 2 | 2.66 |
| 1 | 5.41 |

The modeled polymer properties are presented in Figures 8 through 10. The low shear polymer viscosity corresponding to the injected polymer concentration

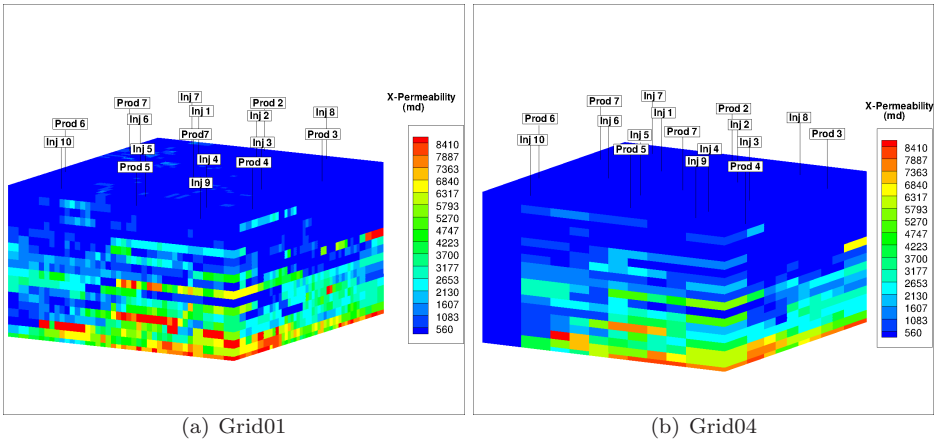


(a) Grid01 (b) Grid04

FIGURE 7. Permeability distribution and well locations for the scale-up case

0.15 $wt\%$ is about 12 $cp$ (Figure 8). The non-Newtonian shear thinning behavior is indicated in Figure 9, where the viscosity is reduced to about 4 $cp$ at shear rate of about 100 $sec^{-1}$. We use a low polymer adsorption of about 7 $\mu g/g$ shown in Figure 10.

The cumulative oil recovery histories are shown in Figures 11 through 13. The cumulative oil recoveries of Grid01(86x94x19) and Grid02(43x47x19) are very close, demonstrating that the areal gridblocks in Grid02 provides adequate resolutions. Simulations with finer areal mesh yield higher oil recovery than those with coarser areal mesh keeping the same vertical resolution as shown in Figure 11. The cumulative oil recoveries for different vertical resolutions keeping the areal resolution the same are shown in Figures 12 and 13 for areal meshes of 43x47 and 22x24 respectively. The cases with fewer vertical layers yield higher oil recovery due to less permeability contrast as a result of property averaging and better vertical equilibrium. The difference in cumulative oil recovery increases at early times of the waterflood and is stable until the polymer flood begins. It then reduces somewhat due to lower injection rates imposed during polymer flood.

The final oil recoveries from waterflood and polymer flood are compared in Figures 14 through 16. These bar plots show that the difference in cumulative oil recovery is more obvious for waterflood than polymer flood, which indicates that even waterflood results show great sensitivity to the choice of the grid as a result of the single-phase upscaling procedure used for reservoir properties.

Figures 17 and 18 show the areal cross sections of oil saturation in the top, middle, and bottom layers at 300 days (end of waterflood) and 600 days (end of water postflush) for Grid02 and Grid04. It is evident that there is more oil left behind at the end of flood for the coarse grid of Grid04 compared to the fine mesh of Grid02.

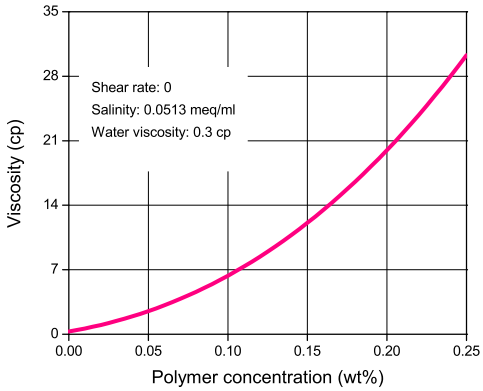


FIGURE 8. Bulk polymer viscosity as a function of polymer concentration

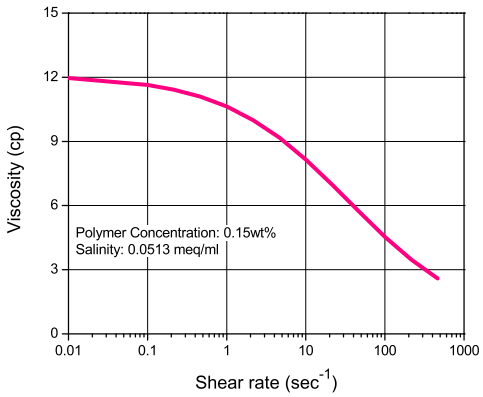


FIGURE 9. Bulk polymer viscosity as a function of shear rate

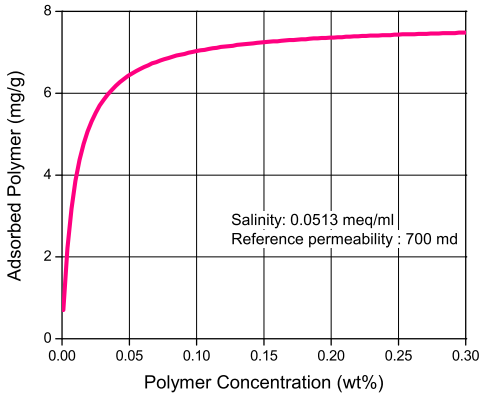


FIGURE 10. Calculated polymer adsorption as a function of polymer concentration

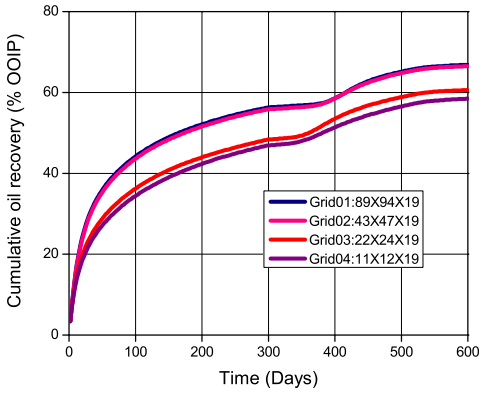


FIGURE 11. Cumulative oil recovery history for grids with the same vertical resolution but different areal resolution

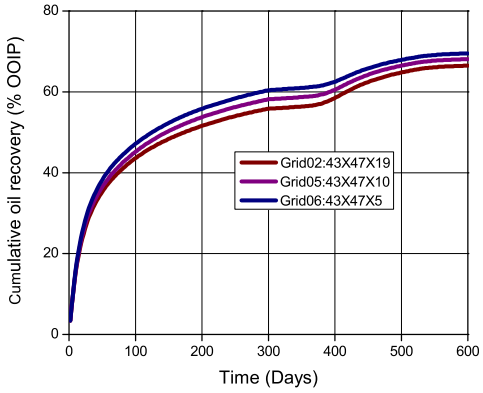


FIGURE 12. Cumulative oil recovery history for grids with different vertical resolution but the same areal mesh of 43x47

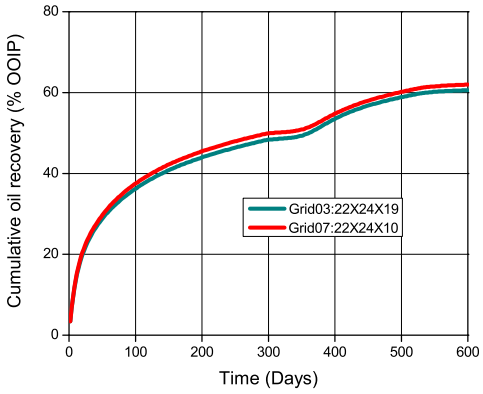


FIGURE 13. Cumulative oil recovery history for grids with different vertical resolution but the same areal mesh of 22x24

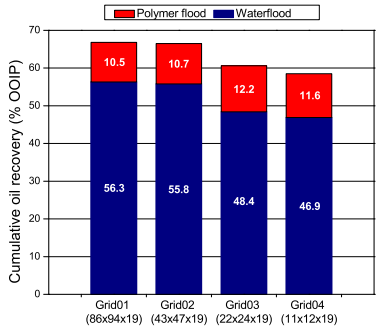


FIGURE 14. Comparison of final oil recoveries from waterflood and polymer flood for grids with the same vertical resolution but different areal resolution

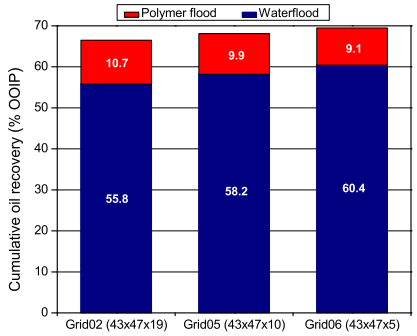


FIGURE 15. Comparison of final oil recoveries from waterflood and polymer flood for grids with different vertical resolution but the same areal mesh of 43x47

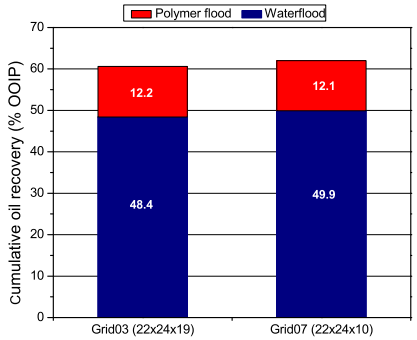


FIGURE 16. Comparison of final oil recoveries from waterflood and polymer flood for grids with different vertical resolution but the same areal mesh of 22x24

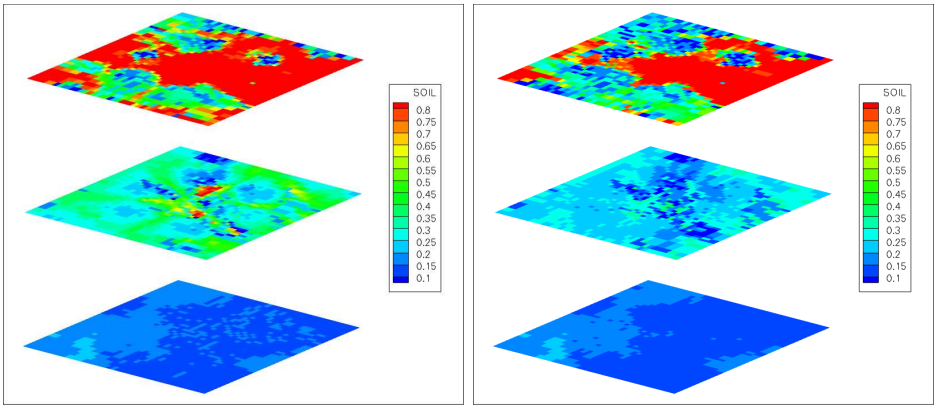


(a) t = 300 days (b) t = 600 days

FIGURE 17. Oil saturation profiles for Grid02 at 300 and 600 days

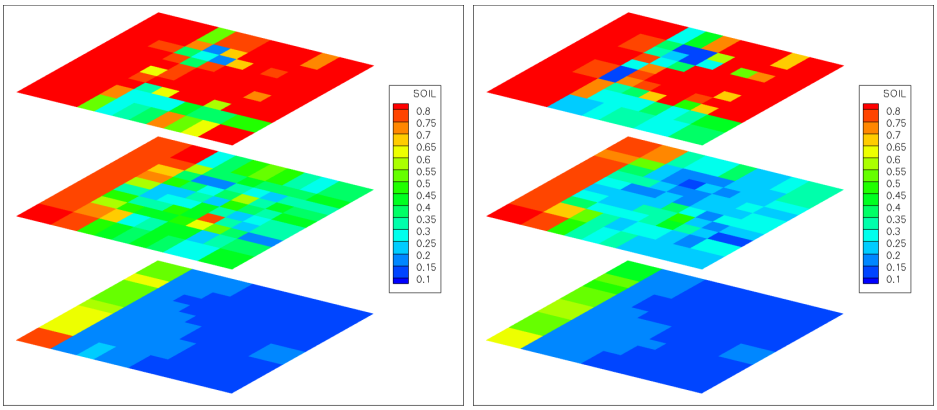


(a) t = 300 days (b) t = 600 days

FIGURE 18. Oil saturation profiles for Grid04 at 300 and 600 days

The oil cut increases significantly after the polymer flood starts regardless of the grid resolution as shown in Figures 19 through 21. Figure 19 indicates that the simulations with coarser areal mesh breakthrough earlier than those with finer areal mesh but same vertical resolution because of larger numerical dispersion associated with larger grid sizes. Figures 20 and 21 show that the oil cut in the grids with more vertical layers increases more than that of the grids with fewer vertical layers after the polymer flood starts. This increase in oil cut confirms that the polymer flood effectively sweeps and produces the oil left by waterflood due to the geological heterogeneity.

The effluent polymer concentration in the producer No. 1 (the central producer) is compared in Figures 22 through 24 for grids with different areal resolutions or different vertical resolutions. Figure 22 shows the earlier breakthrough of polymer in coarse areal mesh as observed in Figure 19. The effluent polymer concentration of the grid with more vertical layers is slightly higher than that of the grid with fewer vertical layers.

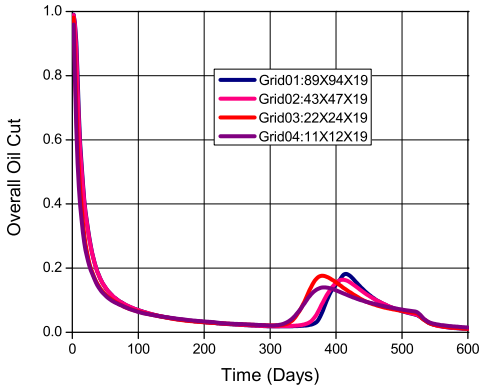


FIGURE 19. Overall oil cut for grids with the same vertical resolution but different areal resolution

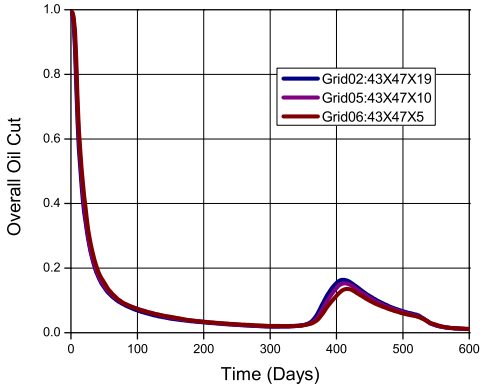


FIGURE 20. Overall oil cut for grids with different vertical resolution but the same areal mesh of 43x47

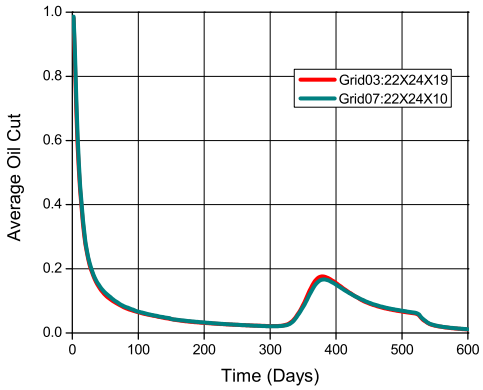


FIGURE 21. Overall oil cut for grids with different vertical resolution but the same areal mesh of 22x24

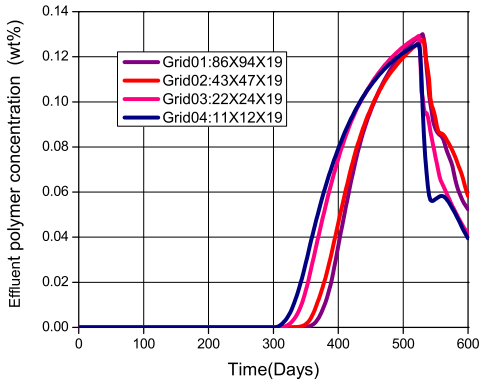


FIGURE 22. Effluent polymer concentration in the producer No. 1 for grids with the same vertical resolution but different areal resolution

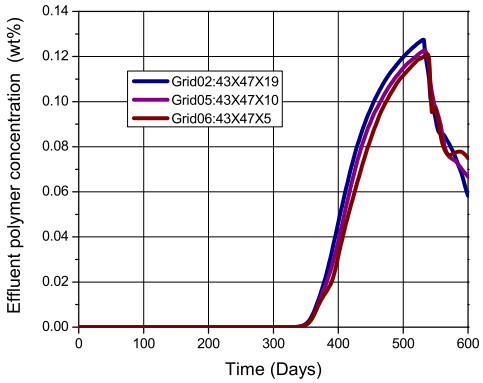


FIGURE 23. Effluent polymer concentration in the producer No. 1 for grids with different vertical resolution but the same areal mesh of 43x47

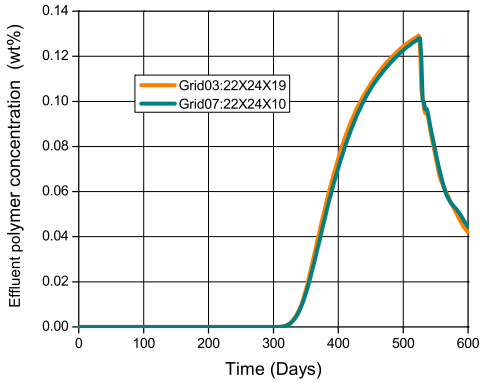


FIGURE 24. Effluent polymer concentration in the producer No. 1 for grids with different vertical resolution but the same areal mesh of 22x24

## 6. Summary and conclusions.

1. Non-Newtonian polymer flow in porous media has been implemented in a multiphase flow and reactive module of IPARS and solved using an efficient time-splitting algorithm to independently solve the advection, diffusion/dispersion, and chemical reactions. To the best of our knowledge, this is the first time that such a comprehensive polymer module has been implemented in a fully implicit parallel reservoir simulator with molecular diffusion and physical dispersion included.
2. Polymer properties modeled include power law viscosity, adsorption, inaccessible pore volume, and permeability reduction.
3. Results were verified against an IMPEC chemical flood simulator,UTCHEM, that has been used in verification of laboratory studies.
4. Fine-scale simulations were performed using up to 16 processors.
5. Simulations with finer grids in areal direction yield higher oil recovery than those with more vertical resolution. The simulations with fewer vertical layers yield higher oil recovery due to less permeability contrast as a result of averaging and better vertical communication.
6. The results indicate that even waterflood results show great sensitivity to the choice of the grid as a result of single phase upscaling procedure for reservoir properties.
7. The timings reported in this paper are not optimal for this highly nonlinear multiphase multicomponent problem. To improve computational accuracy and efficiency, we are currently investigating the use of a posteriori error estimators for the time stepping, Newton and linear system convergence. In addition a better well model for polymer injection with non-Newtonian viscosities is being developed.

**Acknowledgments.** This research is supported by NSF grant 0835745.

## REFERENCES

[1] T. Arbogast, M. Wheeler and I. Yotov, *Mixed finite elements for elliptic problems with tensor coefficients as cell-centered finite differences*, SIAM J. Numer. Anal., **34** (1997), 828–852.
[2] P. Barreau, D. Lasseus, H. Bertin, P. Glenat and Z. Zaitoun, *An experimental and numerical study of polymer action on relative permeability and capillary pressure*, Petroleum Geoscience, **5** (1999), 201–206.
[3] G. Chauveteau, *Rodlike polymer solution flows through fine pores: influence of pore size on rheological behavior*, Journal of Rheology, **26** (1982), 111–142.
[4] C. Dawson and M. Wheeler, *An operator-splitting method for advection-diffusion reaction problems*, in "Mathematics of Finite Elements and Applications VI" (ed. J. R. Whiteman), Academic Press, (1987), 463–482.
[5] R. Dawson and R. Lantz, *Inaccessible pore volume in polymer flooding*, Soc. Pet. Eng. J., **12** (1972), 448–452.
[6] M. Delshad, G. Pope and K. Sepehrnoori, "UTCHEM version 9.0 Technical Documentation," Center for Petroleum and Geosystems Engineering, The University of Texas at Austin, 2000.
[7] P. Flory, "Principles of Polymer Chemistry," Cornell University Press, Ithaca, New York, 1953.
[8] C. Grattoni, P. Luckham, X. Jing, L. Norman and R. Zimmerman, *Polymers as relative permeability modifiers: adsorption and the dynamic formation of thick polyacrylamide layers*, Journal of Petroleum Science & Engineering, **45** (2004), 233–245.
[9] G. Hirasaki and G. Pope, *Analysis of factors influencing mobility and adsorption in the flow of polymer solution through porous media*, Soc. Pet. Eng. J., **14** (1974), 337–346.
[10] C. Huh and G. Pope, *Residual oil saturation from polymer floods: Laboratory measurements and theoretical interpretation*, SPE 113417, 2008.

[11] S. Lacroix, Y. Vassilevski, J. Wheeler and M. Wheeler, *Iterative solution methods for modeling multiphase flow in porous media fully implicitly*, SIAM J. Sci. Comput., **25** (2003), 905–926.
[12] L. Lake, "Enhanced Oil Recovery," Prentice-Hall Inc., Englewood Cliff, NJ, 1989.
[13] E. Lin, "A Study of Micellar/Polymer Flooding Using a Compositional Simulator," Ph.D dissertation, The University of Texas at Austin, 1981.
[14] D. Meter and R. Bird, *Tube flow of non-Newtonian polymer solutions, Parts I: Laminar flow and rheological models*, AICHE J., **10** (1964), 878–881.
[15] M.Peszynska and S. Sun, "Multiphase Reactive Transport Module TRCHEM in IPARSv2," Report num. TICAM01-32, CSM, University of Texas at Austin, 2001.
[16] M. Peszynska, E. Jenkins and M. Wheeler, *Boundary conditions for fully implicit two-phase flow models*, in "Contemporary Mathematics: Recent Advances in Numerical Methods for Partial Differential Equations and Applications" (eds. X. Feng and T. Schultze), American Mathematical Society (2002), 85–106.
[17] K. Sorbie, "Polymer-Improved Oil Recovery," CRC Press Inc., Boca Raton, Florida, 1991.
[18] J. Wheeler *et al.*, "Integrated Parallel and Accurate Reservoir Simulator User's Manual," Center for Subsurface Modeling, The University of Texas at Austin, 2007.
[19] M. Wheeler, G. Pencheva and S. Thomas, "Mortar Coupling of Multiphase Flow and Reactive Transport on Non-Matching Grids," in "Finite Volumes for Complex Applications V (Problems and Prospectives)" (eds. R. Eymard and J. Herard), Aussois, France, **5** (2008), ISBN:978-1-84821-035-6, 135–143.
[20] M. Wheeler, S. Sun and S. Thomas, *Modeling of flow and reactive transport in IPARS*, to appear as a chapter in E-book "Modeling of Reactive Transport in Groundwater," 2009.
[21] G. Willhite and J. Dominguez, "Improved Oil Recovery by Surfactant and Polymer Flooding" (eds. D. Shah and R. Schechter), Academic Press Inc., New York, 1977.
[22] D. Wreath, G. Pope and K. Sepehrnoori *Dependence of polymer apparent viscosity on the permeable media and flow conditions*, In Situ, **14** (1990), 263–284.
[23] C. Zheng, B. Gall, H. Gao, A. Miller and R. Brant, *Effects of polymer adsorption and flow behavior on two-phase flow in porous media*, SPE Reservoir Evaluation & Engineering, **3** (2000), 216–223.

Received January 2010; revised April 2010.

*E-mail address*: clyuan@mail.utexas.edu
*E-mail address*: delshad@mail.utexas.edu
*E-mail address*: mfw@ices.utexas.edu